

Research Article

Thermal Decomposition Behaviour of Foundry Sand for Cast Steel in Nitrogen and Air Atmospheres

Shoukun Chen ¹, Jinjia Zhang ², Kaili Xu ¹ and Qingwei Xu ³

¹Key Laboratory of Ministry of Education on Safe Mining of Deep Metal Mines, School of Resources and Civil Engineering, Northeastern University, Shenyang, China

²Institute of Public Safety Research, Tsinghua University, Beijing, China

³College of Information and Management Science, Henan Agricultural University, Zhengzhou, China

Correspondence should be addressed to Jinjia Zhang; hbzj276@163.com, Kaili Xu; xklsafety@163.com, and Qingwei Xu; xuqingwei1990@163.com

Received 7 April 2020; Accepted 25 May 2020; Published 17 June 2020

Academic Editor: Alessandro Mauro

Copyright © 2020 Shoukun Chen et al. This is an open access article distributed under the Creative Commons Attribution License, which permits unrestricted use, distribution, and reproduction in any medium, provided the original work is properly cited.

Sand casting is the most widely used casting technique, known for ages, even since ancient times. The main goal of this study was to determine the thermal decomposition behaviour of foundry sand for cast steel. We first tested the basic properties of foundry sand, including its proximate analysis, chemical composition, and particle size characteristics; we next monitored the thermal decomposition behaviour of foundry sand for cast steel via simultaneous thermal analysis. We focused on the mass loss of foundry sand for cast steel at different heating rates in nitrogen and air atmospheres. We adopted a novel method to calculate the volatile release characteristic index of foundry sand. The volatile content of foundry sand for cast steel was very low, so the volatile release characteristic index of the sand could not be strictly calculated according to this concept. We calculated the thermal decomposition kinetics parameters of foundry sand, namely, the activation energy and preexponential factor, under kinetics theory. To thoroughly test the fitting effect, we conducted a single-factor analysis of variance on the source of error. The results showed that the independent variable has a significant influence on the dependent variable and that the fitting equation we selected is feasible and effective.

1. Introduction

Since the reform and opening-up policies of recent decades, Chinese industries have rapidly developed [1–3], and the national economy has grown increasingly strong. The foundry industry is the foundation of the manufacturing industry and represents a basic guarantee of innovative, advanced technological equipment; to this effect, it is also an indispensable part of the national economy. China is a good example of a country that is well supported by its foundry industry. Foundry manufacturing is a process for preparing castings by pouring a liquid alloy into a cavity and then solidifying it gradually by refrigeration [4–6]. Despite their contribution to socioeconomic development, foundries also result in significant environmental pollution [7–9] and even casualties [10–12]. Sand casting occupies up to 90% of the

foundry industry [13]. Research regarding the thermal behaviour of sand casting is significant with respect to safe production and casting quality.

The heat conduction that occurs when molten alloy is poured into the cavity causes difficulty in researching sand casting thermal behaviour [14]. The local temperature of foundry sand during alloy casting exceeds 1600°C [15], so it is difficult to measure changes in sand temperature during casting. Numerical simulation is now a common approach to such research [16]; Procast is especially popular for simulating flow, temperature, and stress fields during the casting process [17, 18]. The use of Procast simulations can shorten the production cycle. Zhang, for example, established an inverse conduction model with Procast to determine the heat flux and heat transfer coefficient at the metal-sand mould interface in lost foam casting [18]. Although

Procast can simulate temperature changes during the casting process, it unfortunately is not applicable to the thermal decomposition behaviour of foundry sand.

Previous thermal decomposition characteristics research has mainly centered around coal, wood, rice straw, and rice husk materials [19–21]. Parameters that are significant to the temperature-rise period of the materials (e.g., mass loss, decalescence, and heat release) can be monitored with a thermal analyser, as can the influence of heating rates and thermal decomposition atmospheres on the thermal decomposition characteristics. In addition, dynamic heat and vapor transport in a typical three-dimensional (3D) building structure, involving different types of environment-friendly concrete mixtures, had been simulated by using finite elements [22]. Coronado studied the thermal behaviour of foundry sand dust and monitored the acid gas emissions [23]; however, no previous researcher has investigated the thermal decomposition characteristics of foundry sand for cast steel. We hope to fill this gap.

During the pouring process, the heat conduction phenomena between the molten alloy and casting mould cause the mould temperature to rise rapidly. Foundry sand at the sprue is mainly thermally decomposed in an air atmosphere, and foundry sand in the cavity is mainly thermally decomposed in a nitrogen atmosphere. Therefore, thermal decomposition experiments of foundry sand for cast steel were carried out in air and nitrogen atmospheres, respectively.

The volatile release characteristic index is adopted to represent the pyrolysis behaviour of foundry sand [18]. A larger value indicates better sand release characteristics and a more facile pyrolysis reaction in the sample. To calculate the volatile release characteristic index of foundry sand, it is necessary to determine the initial temperature of volatile emission and mass loss corresponding to a mass loss rate of 0.1 mg/min [19]. The sample mass used for thermal decomposition experiments is usually 5 mg [21]; the initial temperature corresponds to a mass loss rate of 2 wt. % (min). SiO₂ comprises 96.62 wt. % of foundry sand [24], so the volatile content of foundry sand is very low, and the volatile release characteristic index cannot be strictly calculated according to this concept. In this paper, we adopt a novel method to calculate the volatile release characteristic index of foundry sand for cast steel.

The thermal decomposition experiment presented here investigates the physical and chemical characteristics of foundry sand under heating, and thermodynamic and kinetic principles are applied during the research process. The thermal decomposition kinetic parameters include the activation energy and preexponential factor [25]. The activation energy refers to the energy needed for molecules to move from the normal state to an active state that is prone to chemical reaction [26], and the activation energy effectively reflects the stability of the material. The preexponential factor is determined by the thermal decomposition experiment, regardless of the reaction temperature and the concentration of the substance. The activation energy under kinetics theory can be calculated according to thermal decomposition data [27]. In the present study, the thermal decomposition kinetic parameters of foundry sand were calculated according to kinetics theory. After determining the

thermal decomposition kinetics parameters of foundry sand, we roughly determined the fitting effect according to Pearson's R [19, 21]. Xu et al. calculated the thermal decomposition kinetic parameters of foundry sand for cast iron under kinetics theory [27], but they did not test the validity of the calculation results. To rigorously test the fitting effect, we conducted single-factor analysis of variance on the source of error [28].

The main purpose of this study was to investigate the thermal decomposition behaviour of foundry sand for cast steel in nitrogen and air atmospheres. Before the thermal decomposition experiment, some important parameters were tested, such as proximate analysis data and chemical composition. Then, the thermal decomposition curves of foundry sand at different heating rates and atmospheres were analysed in detail. A new method was adopted to calculate the volatile release characteristic index of foundry sand, and its change trends in different heating rates and atmospheres were investigated. The thermal decomposition kinetics parameters of foundry sand were calculated under kinetics theory, and single-factor analysis of variance was carried out to test the validity of the calculation results.

2. Materials and Methods

2.1. Foundry Sand for Cast Steel

2.1.1. Proximate Analysis. The foundry sand for cast steel that we used in this experiment was obtained from a research institute in Shenyang, China. We performed proximate analysis of the sample to ensure comprehensive investigation of its thermal decomposition behaviour in a high-temperature environment (TRGF-8000 Automatic Proximate Analyzer, Electronic and Technology Co., Ltd., of Tianrun Hebi, China). The foundry sand we tested is mainly composed of ash (98.82 wt. %), volatiles (2.15 wt. %), and moisture (0.03 wt. %). The fixed carbon content of the foundry sand was not detectable. The ash fraction indicates incombustible substances, or the residual offscourings after a given substance are completely burned. The main composition of foundry sand is ash, indicating that foundry sand is stable at high temperatures.

2.1.2. Chemical Composition Analysis. The chemical composition of the foundry sand mainly includes SiO₂. We determined the chemical composition of the sand on a ZSX Primus X-ray fluorescence (XRF) device (Rigaku Co., Japan). The XRF results are shown in Table 1.

One of the most important properties of foundry sand is stability at high temperatures [29–31]. The chemical composition of the foundry sand is mainly SiO₂, indicating that the foundry sand is stable at high temperatures. The chemical composition analysis results of the foundry sand were consistent with the proximate analysis.

2.2. Thermal Decomposition Experiments. We conducted thermogravimetric analysis of the foundry sand on an STA449 F3 sensitive thermal balance (NETZSCH Group, Germany). The thermogravimetric (TG) curve was

TABLE 1: Chemical composition of foundry sand.

Chemical composition	wt. %	Chemical composition	wt. %
SiO ₂	94.6021	MgO	0.0530
Fe ₂ O ₃	1.9775	Na ₂ O	0.0526
Al ₂ O ₃	1.1150	ZrO ₂	0.0418
SO ₃	0.8141	CuO	0.0372
K ₂ O	0.5864	ZnO	0.0221
Cr ₂ O ₃	0.2576	P ₂ O ₅	0.0190
CaO	0.2152	PbO	0.0178
MnO	0.1082	NiO	0.0136
TiO ₂	0.0637	Rb ₂ O	0.0032

measured to obtain the weight loss, and a differential scanning calorimeter (DSC) was used to obtain phase transitions. The first derivative of the TG profile, that is, derivative thermogravimetric (DTG) curve, was used to obtain the weight loss rate.

We conducted thermal decomposition experiments in a nitrogen atmosphere at heating rates of 20, 30, and 40°C/min and in an air (oxygen: nitrogen = 1: 4) atmosphere at a heating rate of 20°C/min. The thermal decomposition characteristics of foundry sand at temperatures above 100°C were the focus of this experiment due to the rapid temperature increase in foundry sand during pouring of the liquid alloy into the cavity; the temperature range of the thermal decomposition experiments was from 35°C to 1100°C. One sample was measured in each iteration of the experiment. The statistical data supporting this paper can be found in the electronic supplementary materials.

2.3. Volatile Release Characteristic Index. The volatile release characteristic index was adopted to represent the pyrolysis behaviour of foundry sand [18]. A larger value indicates better sand release characteristics and a more facile pyrolysis reaction in the sample. The calculation procedures of the volatile release characteristic index were as follows.

Without regard to moisture release in the initial stage and inorganic salt decomposition in the later period, the volatile release characteristic index D is calculated as follows:

$$D = \frac{(dw/d\tau)_{\max} (dw/d\tau)_{\text{mean}}}{T_s T_{\max} \Delta_{1/2}}, \quad (1)$$

where T_s indicates the initial temperature of volatile emission and mass loss corresponding to a mass loss rate of 0.1 mg/min [19] in °C. T_{\max} indicates the temperature corresponding to the maximum mass loss rate in °C. $(dw/d\tau)_{\text{mean}}$ indicates the mean mass loss rate of volatiles in wt. % (min). $(dw/d\tau)_{\max}$ indicates the maximum mass loss rate of volatiles in wt. % (min), and $\Delta_{1/2}$ indicates the temperature interval within the scope of $(dw/d\tau)/(dw/d\tau)_{\max} = 1/2$ in °C.

2.4. Kinetic Theory. The thermal decomposition data obtained under different heating rates and atmospheres can be used for the determination of pyrolysis reaction kinetics. The integral Coats-Redfern method, which has been successfully employed for investigations of the pyrolysis kinetic

parameters, was employed for mathematical analysis [25]. The degradation rate is defined according to the equation of an Arrhenius-type kinetic model, and first-order-reaction-based Arrhenius theory is commonly employed in the kinetic analysis of pyrolysis [26].

The kinetic theory of the thermal decomposition of foundry sand is based on the rate of conversion [32]:

$$\frac{d\alpha}{dt} = k(T)f(\alpha), \quad (2)$$

where $d\alpha/dt$ denotes the conversion rate, calculated from the rate constant based on temperature $k(T)$ and the reaction function $f(\alpha)$.

The parameter α denotes the conversion of the reaction process:

$$\alpha = \frac{m_0 - m_t}{m_0 - m_\infty}, \quad (3)$$

where m_0 , m_∞ , and m_t denote the initial mass of the sample, the final mass of the sample, and the mass of the sample at a specific time t , respectively.

The rate constant of foundry sand based on the first-order reaction is described as follows under the Arrhenius law [33]:

$$k(T) = A \exp\left(-\frac{E}{RT}\right), \quad (4)$$

where A denotes the preexponential factor, min^{-1} ; E denotes the activation energy, KJ/mol; R denotes the universal gas constant, 8.314 J/mol/K; and T denotes the thermodynamic temperature, K.

The reaction function is expressed as follows [34]:

$$f(\alpha) = 1 - \alpha. \quad (5)$$

For a constant heating rate $\beta = dT/dt$, the heating rate and equations (4) and (5) can be inserted into equation (2), which can then be rewritten as follows:

$$\frac{d\alpha}{dT} = \frac{A}{\beta} \exp\left(-\frac{E}{RT}\right) (1 - \alpha). \quad (6)$$

The following equation can be obtained based on the Coats-Redfern method [34]:

$$-\ln\left[\frac{-\ln(1 - \alpha)}{T^2}\right] = \frac{E}{RT} - \ln\left[\frac{AR}{\beta E} \left(1 - \frac{2RT}{E}\right)\right]. \quad (7)$$

The term $2RT/E$ is far less than 1 and can be neglected, so equation (7) can be simplified as follows:

$$-\ln\left[\frac{-\ln(1 - \alpha)}{T^2}\right] = \frac{E}{RT} - \ln\left(\frac{AR}{\beta E}\right). \quad (8)$$

For a given heating rate, the term $-\ln[-\ln(1 - \alpha)/T^2]$ varies linearly as $1/T$ with a slope of E/R ; the intercept is $-\ln(AR/\beta E)$. The pyrolysis kinetic parameters, namely, activation energy E and preexponential factor A , can be calculated by equation (8).

2.5. Single-Factor Analysis of Variance. Single-factor analysis of variance is a commonly used statistical approach to

analyse the sources of error in data. The goal of single-factor analysis of variance is to determine whether the independent variable has a significant influence on the dependent variable by comparing the average of multiple normal distribution samples for equality [28].

Let factor A have r levels, that is, A_1, A_2, \dots, A_r ; x_{ij} indicates the j th observed value of the i th level. The specific procedures of single-factor analysis of variance are as follows [28].

First, two assumptions are made:

H_0 : $\mu_1 = \mu_2 = \dots = \mu_k$, indicating that the factor has less of an effect on the experimental results than does random error

H_1 : $\mu_1, \mu_2, \dots, \mu_k$ are not completely the same, indicating that the factor has a greater effect on the experimental results than does random error

Then, calculate the average value of the factor at different levels as follows:

$$\bar{x}_i = \frac{\sum_{j=1}^{n_i} x_{ij}}{n_i}, \quad i = 1, 2, \dots, k, \quad (9)$$

where n_i indicates the total quantity of experimental data points.

The average value of the factor at all levels can be determined as follows:

$$\bar{\bar{x}} = \frac{\sum_{i=1}^k \sum_{j=1}^{n_i} x_{ij}}{n} = \frac{\sum_{i=1}^k n_i \bar{x}_i}{n}, \quad (10)$$

where $n = n_1 + n_2 + \dots + n_k$.

To construct a statistical test, it is also necessary to calculate the total error sum of squares SST, factor error sum of squares SSA, and random error sum of squares SSE:

$$\begin{aligned} \text{SST} &= \sum_{i=1}^k \sum_{j=1}^{n_i} (x_{ij} - \bar{\bar{x}})^2, \\ \text{SSA} &= \sum_{i=1}^k \sum_{j=1}^{n_i} (\bar{x}_i - \bar{\bar{x}})^2 = \sum_{i=1}^k n_i (\bar{x}_i - \bar{\bar{x}})^2, \\ \text{SSE} &= \sum_{i=1}^k \sum_{j=1}^{n_i} (x_{ij} - \bar{x}_i)^2. \end{aligned} \quad (11)$$

The relationship among SST, SSA, and SSE is as follows:

$$\text{SST} = \text{SSA} + \text{SSE}. \quad (12)$$

These three error sums of squares are affected by the number of observations. The error sum of squares is larger when there are more observations. It is necessary to divide the error sum of squares by the corresponding degrees of freedom to eliminate the effect of observation quantity on the error sum of squares to determine the mean squares. The degrees of freedom for SST, SSA, and SSE are $n-1$, $k-1$, and $n-k$, respectively.

The mean square of SSA is the ‘‘model mean square,’’ MSA, which can be calculated as follows:

$$\text{MSA} = \frac{\text{SSA}}{k-1}. \quad (13)$$

The mean square of SSE is the ‘‘error mean square,’’ MSE, which can be calculated as follows:

$$\text{MSE} = \frac{\text{SSE}}{n-k}. \quad (14)$$

The ratio of MSA to MSE obeys the F -distribution and is written as follows:

$$F = \frac{\text{MSA}}{\text{MSE}} \sim F(k-1, n-k). \quad (15)$$

The calculation results are shown in Table 2.

Next, the critical value $F_\alpha(k-1, n-k)$ is determined according to the significance level α and F -distribution tables. Statistical decisions are made according to the test statistics F and critical value $F_\alpha(k-1, n-k)$. H_0 is rejected if $F > F_\alpha$, which indicates that the factor has a greater effect on the experimental results than does random error. H_0 is accepted if $F < F_\alpha$, which indicates that the factor has less of an effect on the experimental results than does random error.

3. Results and Discussion

3.1. Proximate Analysis of Foundry Sand. There is no previously published literature regarding the proximate analysis of foundry sand. Previous experimental materials submitted to proximate analysis include mainly coal, wood, rice straw, and rice husk [19–21]. The range of fixed carbon in coal varies widely, mainly because the metamorphic grade of different coal types differs. The fixed carbon content of foundry sand in this study was not detectable, indicating that pulverized coal was not added during the sand mixing process.

In contrast to other materials, such as coal, wood, rice straw, and rice husk [19–21], the main composition of foundry sand is ash. When pouring alloy metal into the cavity of a foundry, the adhesives, curing agents, and coatings in the sand quickly vaporize and pyrolyze, and the remaining substance is mainly ash. The greater the ash content, the more stable the material.

3.2. Chemical Composition Analysis of Foundry Sand. The XRF results indicate that there were 18 chemical components in the foundry sand, in which the content of SiO_2 (94.6021 wt. %) was the largest; the main component was SiO_2 according to the proximate analysis. The SiO_2 content of silica sand can be as high as 96.62 wt. % [24]. Other materials (e.g., resin) were added in the process of sand mixing, which decreased the SiO_2 content to some extent. A small amount of Fe_2O_3 was added to improve the high-temperature strength of the foundry sand. The chemical composition of foundry sand dust was tested, and the content of SiO_2 was only 50 wt. % [23]. Many impurities

TABLE 2: Single-factor analysis of variance.

Source of variation	Sum of squares	Degrees of freedom	Mean square	F	Probability
Model error	SSA	$k - 1$	MSA	MSA/MSE	$p = P\{F > (MSA/MSE)\}$
Random error	SSE	$n - k$	MSE		
Total error	SST	$n - 1$			

were introduced into the foundry sand dust in the process of sand shakeout, which drastically reduced SiO_2 .

The chemical composition of foundry sand mainly includes SiO_2 , and SiO_2 is stable in high-temperature environments, which will benefit the maintenance of the shape of the casting mould.

3.3. Thermal Decomposition Behaviour of Foundry Sand in a Nitrogen Atmosphere. The mass of foundry sand gradually decreases during thermal decomposition, accompanied by heat absorption or release. The thermal decomposition data for foundry sand in nitrogen atmosphere can be found in Supplementary Materials S1, S2, and S3. The thermogram of our foundry sand sample at a heating rate of $20^\circ\text{C}/\text{min}$ in a nitrogen atmosphere is shown in Figure 1.

In Figure 1, “TG” denotes “thermogravimetric,” “DTG” is “derivative thermal gravimetric,” and “DSC” is “differential scanning calorimetry.” A downward DSC curve indicates heat release, and an upward curve indicates the absorption of heat.

As shown in Figure 1, the thermal decomposition of foundry sand can be divided into three stages. The first mass loss stage mainly occurred below 220°C , where the sand mass slowly decreased. The DSC curve shows an endothermic state, but no obvious endothermic peak appears. The thermal decomposition results of foundry sand dust indicated an endothermic peak in the DSC curve at 127°C due to the release of absorbed water [23]. The moisture content of foundry sand in this study was as low as 0.03 wt. %; there was no obvious endothermic peak corresponding to the release of moisture during thermal decomposition.

The second mass loss stage took place from 220°C to 800°C , where volatile devolatilization occurred. There is an endothermic peak at 573°C due to the transformation of quartz from the β to the α phase. The binding resin was pyrolyzed to produce gas molecules such as CH_4 and CO in this stage. The mass loss in this pyrolysis phase substantially contributed to the total mass loss, approximately 81 wt. %. Foundry sand dust was in an endothermic state at temperatures above approximately 200°C in an air atmosphere in a previous report [23], but our results were dissimilar. This difference was mainly due to the oxidation or combustion of impurities in the foundry sand dust sample. The thermal decomposition of our sand was mainly attributable to its binding agent, and there was no obvious oxidation or combustion reaction in the nitrogen atmosphere.

The third thermal decomposition stage mainly took place above 800°C . The remaining binding agent continued to decompose slowly, and the mass loss rate of the foundry sand was significantly reduced.

Interestingly, no flat region can be identified in the DSC curve in Figure 2. In other words, the foundry sand did not reach steady state by the final temperature of this experiment. The DSC curves of corncob show similar rising trends at a final temperature of 1200°C at $5^\circ\text{C}/\text{min}$ and $20^\circ\text{C}/\text{min}$ heating rates [34]. The DSC curve of rice husk has a downtrend at the final temperature of 1200°C at a $20^\circ\text{C}/\text{min}$ heating rate [21]. The magnitude of the peak also appears to be unrelated to the magnitude of the DSC curve at the final temperature. In corncob, the peak magnitude is greater than the DSC curve magnitude at the final temperature [34], but the peak magnitude of rice husk is less than the DSC curve magnitude at the final temperature [21]. Four different diameters of corncob particles were used to investigate the effects of particle size on thermal decomposition behaviour [34]; all four samples exhibited downtrends in the DSC curves at the final temperature [34].

CO released by pyrolysis of binding resin may result in poisoning and asphyxiation accidents [35]. CO easily binds with haemoglobin to form carbonyl haemoglobin, which causes the haemoglobin to lose its ability to carry oxygen, leading to suffocation [36, 37]. CO has toxic effects on the whole body, especially on the cerebral cortex [38, 39]. Therefore, corresponding safety measures should be adopted to prevent such accidents, such as improving safety management practices, identifying dangerous and harmful factors, and eliminating accident potential.

3.4. Thermal Decomposition of Foundry Sand in Nitrogen and Air Atmospheres. The thermal decomposition data for foundry sand in nitrogen and air atmospheres can be found in Supplementary Materials S1, S2, S3, and S4. The thermal decomposition behaviours of foundry sand at a $20^\circ\text{C}/\text{min}$ heating rate in nitrogen and air atmospheres are shown in Figure 2.

As shown in Figure 2, the mass of foundry sand gradually decreased as the temperature increased in both the nitrogen and air atmospheres. Above 600°C , the mass of the sand basically remained unchanged. The mass loss of foundry sand was greater in air than in nitrogen, mainly due to the binding agent in the foundry sand being prone to pyrolysis in an air atmosphere. The mass loss of plywood is also higher in air than in nitrogen [20].

The mass loss rate of foundry sand from 250°C to 600°C was much larger in the air atmosphere than in the nitrogen atmosphere, but beyond this range, the rates were almost the same. The mass loss rate of foundry sand was the highest at approximately 450°C , and the thermal decomposition was the most severe at this time. The sand binding agent used in this study was furan resin. Methylene or methine bridges connecting furan resin chains begin to break at temperatures

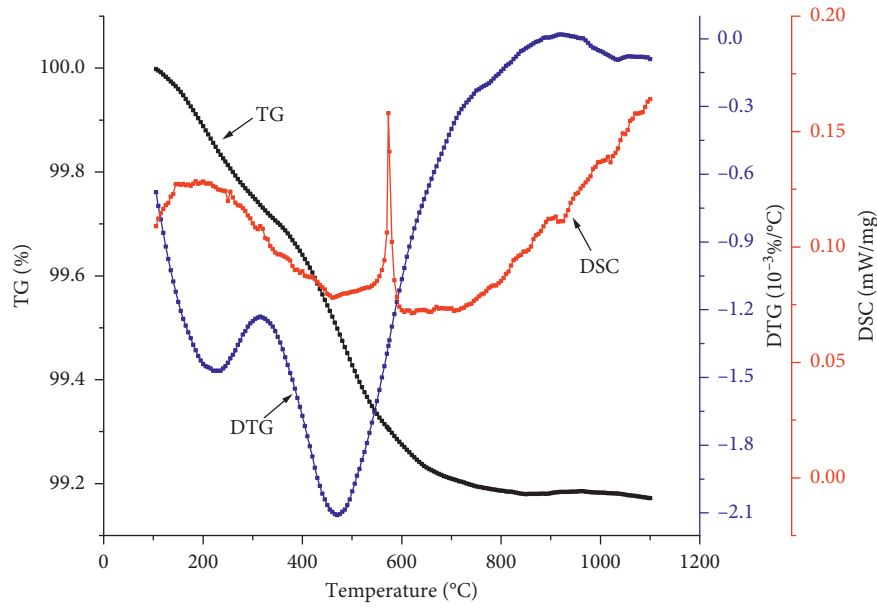


FIGURE 1: Thermogram of foundry sand in nitrogen atmosphere.

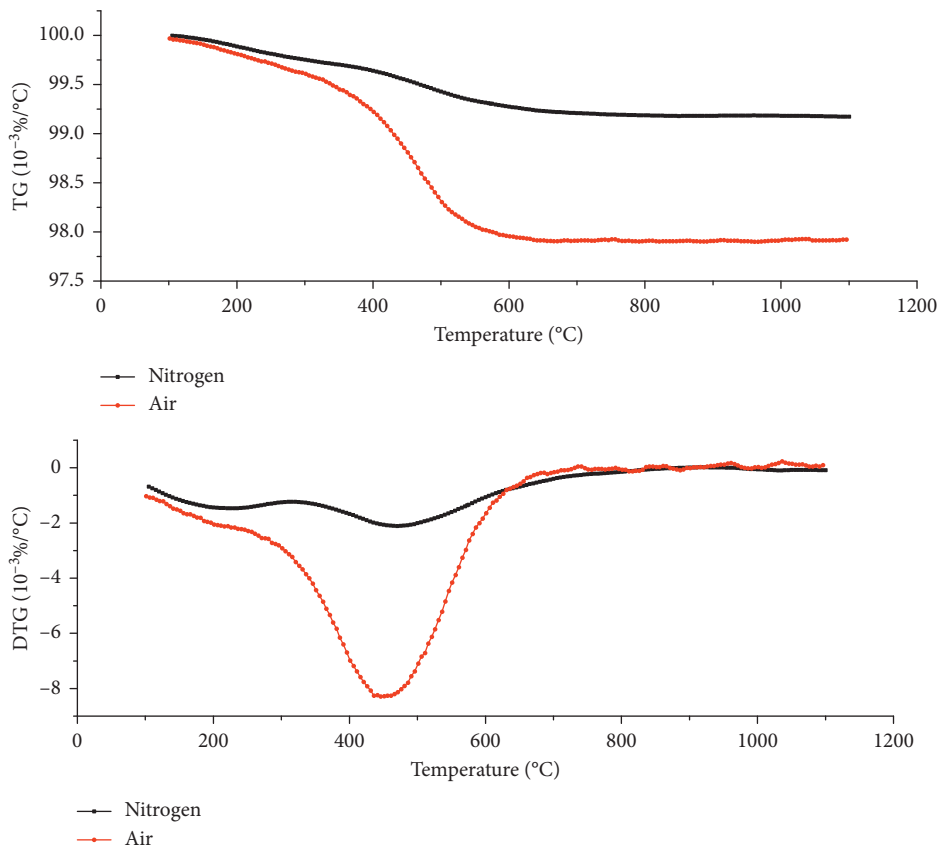


FIGURE 2: Thermograms of foundry sand in nitrogen and air atmospheres.

exceeding 250°C [40]. Furan resin undergoes significant ring-opening reactions between 300°C and 350°C [40]. Benzene may also be formed from the fragments derived from said ring-opening reactions; in our experiment, the amount of benzene significantly increased starting at 400°C

[41]. From 460°C to 650°C, benzene formed from the furan resin-derived intermediates [42].

In a previous study, Xu et al. only investigated the thermal composition characteristics of foundry sand for cast iron in a nitrogen atmosphere [27]. Foundry sand at the

sprue is mainly thermally decomposed in an air atmosphere, and foundry sand in the cavity is mainly thermally decomposed in a nitrogen atmosphere. This study investigated the thermal composition characteristics of foundry sand in air and nitrogen atmospheres, which enriches the theoretical knowledge base related to foundry sand.

3.5. Thermal Decomposition of Foundry Sand at Different Heating Rates. Foundry sand binding agents have different thermal conditions and different pyrolysis behaviours at different heating rates. The thermal composition behaviours of foundry sand at heating rates of 20, 30, and 40°C/min in a nitrogen atmosphere are shown in Figure 3.

As shown in the TG curves in Figure 3, the mass loss of foundry sand increased as the heating rate increased. The mass loss of foundry sand was 0.83 wt. % at a heating rate of 20°C/min but reached 0.99 and 1.36 wt. % at heating rates of 30°C and 40°C/min, respectively. An elevated heating rate appears to enhance the thermal decomposition of foundry sand in a high-temperature environment. The mass loss of corncob and peanut shells also increases as the heating rate increases [34, 43]. The main component of foundry sand, SiO₂, has high-temperature stability. Therefore, the mass loss of foundry sand is relatively small in a high-temperature environment, which benefits sand casting moulding.

As shown in the DTG curves in Figure 3, the mass loss rate of foundry sand increased as the heating rate increased. The maximum mass loss rate was -2.33×10^{-3} % (°C) at a heating rate of 20°C/min but reached -3.27×10^{-3} and -5.42×10^{-3} % (°C) at heating rates of 30°C and 40°C/min, respectively. Again, increasing the heating rate apparently enhances the thermal decomposition of foundry sand in a high-temperature environment. The maximum mass loss rate of peanut shell increased twofold to threefold as the heating rate increased in a previously published study [43], which is consistent with our results. The peak temperature of the DTG curve also increased as the heating rate increased. The maximum peak temperatures were 470, 472, and 485°C at heating rates of 20, 30, and 40°C/min, respectively. This thermal hysteresis was mainly caused by the temperature gradient between the support and the sample as well as between the inside and outside of the sample [34].

The mass loss of foundry sand trended downward as the heating rate increased. Generally, a slower heating rate results in greater mass loss of a material (e.g., bituminous coal) [44]. The main reason for this phenomenon is that a slower heating rate means longer exposure to elevated temperature and a longer thermal decomposition time. For the resin in this study, increasing the heating rate not only truncated the initial decomposition reaction time but also promoted the pyrolysis reaction [45]. The binding agent we used was furan resin, as mentioned above. Chen and Yeh reported that the residual mass fraction of resin trends down as the heating rate increases [46], which is consistent with our observations. A faster heating rate results in a faster resin decomposition rate, a greater amount of decomposition, and less crosslinking charring.

Xu et al. only investigated the thermal composition characteristics of foundry sand for cast iron at heating rates of 30°C and 40°C/min [27]. Increasing the heating rate appears to enhance the thermal decomposition of foundry sand in a high-temperature environment [27], which was consistent with our study. However, this study investigated the thermal composition characteristics of foundry sand at heating rates of 20, 30, and 40°C/min, and our conclusion is more persuasive.

3.6. Volatile Release Characteristic Index of Foundry Sand. The volatile release characteristic index D of foundry sand can be determined according to the thermal decomposition process. The initial temperature T_s of volatile emission and mass loss is first established by reference to a mass loss rate of 0.1 mg/min [19]. The sample mass is usually 5 mg when carrying out a thermal decomposition experiment [21], so the initial temperature T_s corresponds to a mass loss rate of 2 wt. % (min). The initial temperature T_s is unrelated to the mass of the sample after it is rewritten as mass loss percent per minute. In this study, the maximum mass loss of foundry sand was 1.36 wt. % in the nitrogen atmosphere and 2.08 wt. % in the air atmosphere, and the maximum mass loss rate was 0.2 wt. % (min) in the air atmosphere. The volatile release characteristic index D thus cannot be calculated according to this concept, as discussed above. To solve this issue, Xu et al. [27] proposed that the term T_{stv}/m_{loss} be 2.86 wt. %/min, where T_{stv} indicates the threshold value for determining T_s .

The volatile release characteristics of foundry sand for cast steel were determined, as shown in Table 3.

As shown in Table 3, the volatile release characteristic index of foundry sand increased as the heating rate increased, indicating that an elevated heating rate benefits the thermal decomposition of foundry sand in a high-temperature environment. The mass loss of corncob also increases as the heating rate increases [34]. The results were consistent at different heating rates in the nitrogen atmosphere. The volatile release characteristic index of foundry sand in the air atmosphere was one order of magnitude larger than that in the nitrogen atmosphere, mainly because the sand binding agent is more prone to pyrolysis in air than in nitrogen. The results between nitrogen and air atmospheres were consistent.

Compared to other materials, the volatile release characteristic index of foundry sand is approximately 1/100,000th that of rice straw [21], 1/1,000th that of corncob [34], one-millionth that of wastewater solids, and 1/1,000th that of lignite [33]. Foundry sand evaporates less quickly than other materials, mainly because its volatile content is only approximately 2.15 wt. %. The main component of foundry sand, SiO₂, has high-temperature stability. These results are consistent with our proximate analysis and TG curve analysis.

3.7. Thermal Decomposition Kinetics Analysis of Foundry Sand. The variations between $-\ln[-\ln(1-\alpha)/T^2]$ and $(1/T) \times 10^3$ at a heating rate of 20°C/min in nitrogen and air atmospheres are shown in Figure 4.

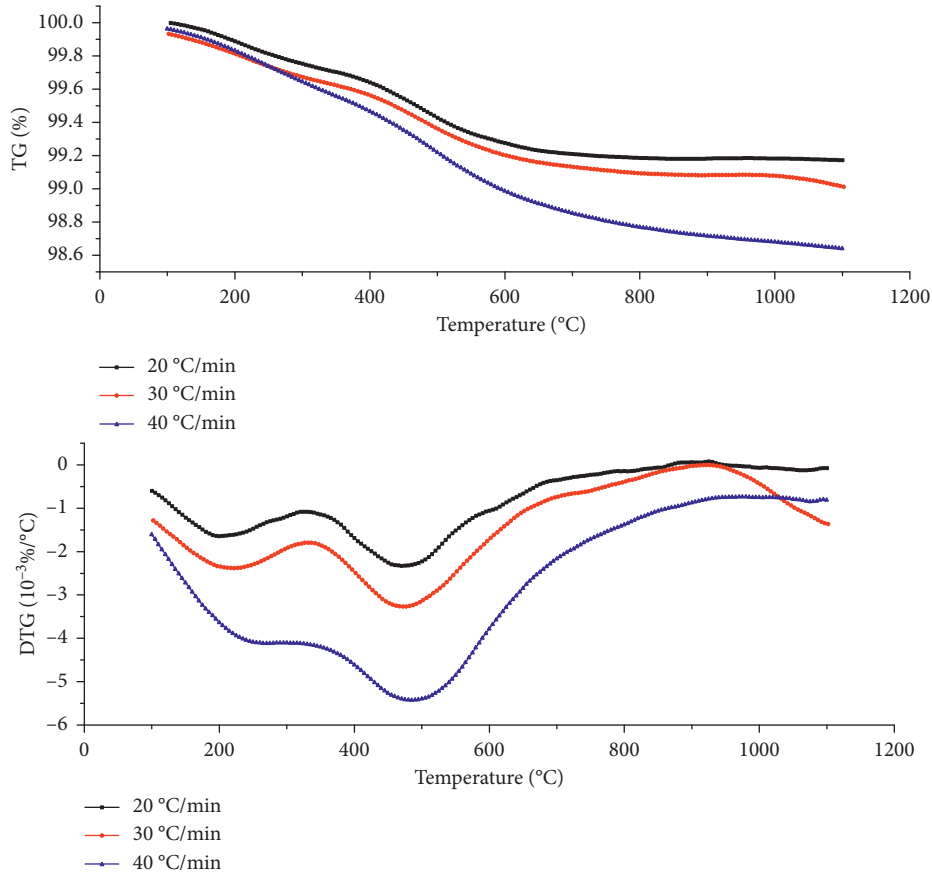


FIGURE 3: Thermal decomposition of foundry sand at heating rates of 20°C, 30°C, and 40°C/min.

TABLE 3: Volatile release characteristics of foundry sand.

Atmosphere	β (°C/min)	T_{stv} (wt. % (min))	m_{loss} (wt. %)	T_s (°C)	T_{max} (°C)	$(dw/d\tau)_{mean}$ (wt. % (min))	$(dw/d\tau)_{mean}$ (wt. % (min))	$\Delta_{1/2}$ (°C)	D (wt. % ² (min ²)/°C ³)
Nitrogen	20	2.37×10^{-2}	0.83	153	471	4.22×10^{-2}	1.56×10^{-2}	463	1.97×10^{-11}
Nitrogen	30	2.80×10^{-2}	0.98	115	473	6.58×10^{-2}	2.76×10^{-2}	483	6.91×10^{-11}
Nitrogen	40	3.89×10^{-2}	1.36	126	492	1.20×10^{-1}	5.11×10^{-2}	468	2.11×10^{-10}
Air	20	5.92×10^{-2}	2.07	310	460	1.89×10^{-1}	3.89×10^{-2}	172	3.00×10^{-10}

The activation energy E and preexponential factor A can be calculated by equation (8), as shown in Figure 4 and Table 4.

In Table 4, the temperature range 390°C–530°C corresponds to the main volatile release phase. After obtaining the fitting equation for the independent and dependent variables, the fitting effect can be roughly determined by Pearson's R. To thoroughly test the fitting effect, single-factor analysis of variance is needed to determine the source of error (Table 5).

$F_{0.05}(1, 27) = 4.21 < 1877$ was determined from F -distribution tables and $p = 0 < 0.05$. We found that the independent variable has a significant influence on the dependent variable in nitrogen and air atmospheres. The single-factor analysis of variance results also showed that the selected fitting equation is feasible and effective.

As shown in Table 4, the calculated thermal decomposition activation energy was higher in the air atmosphere

than in the nitrogen atmosphere due to the presence of oxygen. Previous researchers have made similar observations [20, 47, 48] regarding high activation energy in oxidizing atmospheres. Regarding the thermal decomposition analysis of powdered ammonium nitrate, Yang [49] concluded that the activation energy was lower in air than in nitrogen. Previous scholars have calculated thermodynamic and kinetic parameters for atmospheres with varying oxygen concentrations to determine the change trend of activation energy parameters [50, 51]; the activation energy does not increase or decrease strictly with increases in oxygen concentration. The activation energy may increase steadily with concentration until reaching a maximum and then decrease [27, 52].

Compared to other materials, the activation energy of foundry sand was approximately one-third that of peanut shells [43], one-fourth that of corncob [34], 1/19th that of coal, and 1/10th that of wastewater solids [33]. Foundry sand

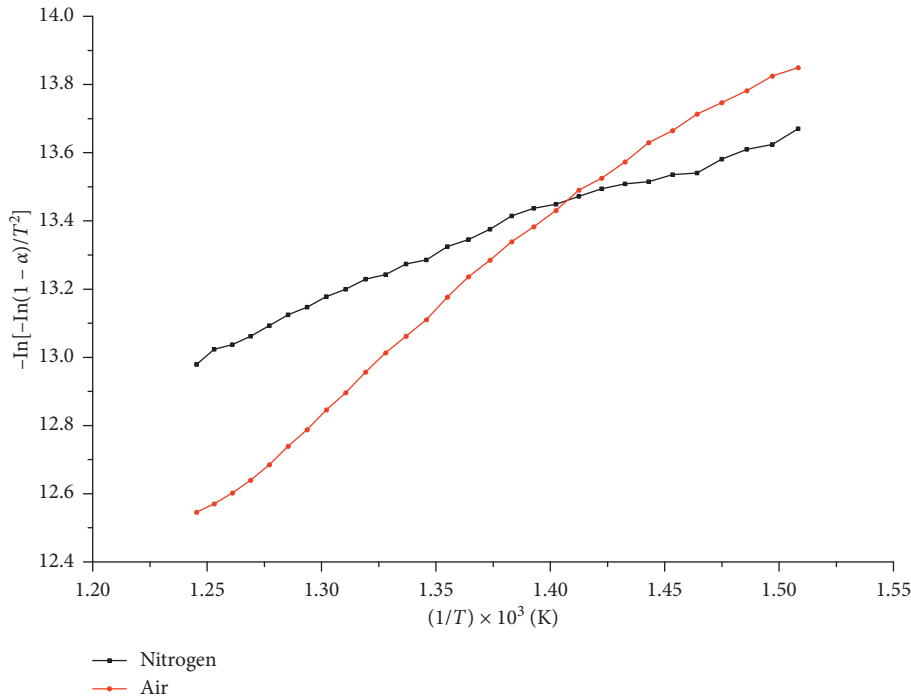


FIGURE 4: Relationship between $-\ln[-\ln(1-\alpha)/T^2]$ and $(1/T) \times 10^3$.

TABLE 4: Thermal decomposition kinetics parameters of foundry sand.

Atmosphere	Temperature range (°C)	Fitting equation	E (KJ/mol)	A (min^{-1})	Pearson's R
Nitrogen	390–530	$y = 2.5182x + 9.8902$	20.94	2.55×10^{-3}	0.99288
Air	390–530	$y = 5.2915x + 5.9679$	43.99	0.27	0.99569

TABLE 5: Single-factor analysis of variance results.

Atmosphere	Source of variation	Sum of squares	Degrees of freedom	Mean square	F	Probability
Nitrogen	Model error	1.13	1	1.13	1877	0
	Random error	1.63×10^{-2}	27	6.03×10^{-4}		
	Total	1.15	28			
Air	Model error	4.99	1	4.99	3110	0
	Random error	4.34×10^{-2}	27	1.61×10^{-3}		
	Total	5.04	28			

has high-temperature stability, as confirmed by the volatile release characteristic index: a great deal of activation energy is needed to convert volatiles into an active state. The activation energy of foundry sand is relatively small, however, which seems to contradict the volatile release characteristic index. This result is mainly due to the wide temperature range of thermal decomposition of the sand. Weight loss occurring between 390°C and 530°C in our sample (i.e., within the activation energy zone we calculated) contributed approximately 38 wt. % of the total weight loss. The weight loss of corncob in the pyrolysis zone contributes approximately 80 to 90 wt. % of the total weight loss [34].

Severe heat conduction phenomena occur when molten alloy is poured into the cavity of the foundry [15], resulting in the temperature of the casting mould rapidly rising. For sand

casting, as the temperature of the casting mould rises, materials such as adhesives, curing agents, and coatings in the sand quickly vaporize and pyrolyze to produce gas [4, 27]. If the gas cannot be discharged out of the cavity in time, there may be a blowhole defect or even an explosion accident [15]. Therefore, investigating the thermal decomposition behaviour of foundry sand is helpful for obtaining an in-depth understanding of the change trends in casting mould temperature and cavity gas during the pouring process.

4. Conclusion

We investigated the thermal decomposition behaviour of foundry sand for cast steel in air and nitrogen atmospheres for the first time in this study, and the heating rates were 20,

30, and 40°C/min. Our conclusions can be summarized as follows.

Proximate analysis and chemical composition analysis of foundry sand indicate that foundry sand has stability in high-temperature environments, which will benefit the maintenance of the shape of the casting mould. The thermal decomposition of foundry sand was mainly attributable to its binding agent, and there was no obvious oxidation or combustion reaction of the sand in the nitrogen atmosphere.

The change trends for the thermal decomposition of foundry sand can be determined by changing the thermal decomposition environment. The mass loss of foundry sand was greater in air than in nitrogen, mainly due to the binding agent of foundry sand being prone to pyrolysis in the air atmosphere. In addition, an elevated heating rate appears to enhance the thermal decomposition of foundry sand in a high-temperature environment.

To determine the volatile release characteristic index of foundry sand, a new method was adopted. The volatile release characteristic index of foundry sand increased as the heating rate increased, indicating that an elevated heating rate benefits the thermal decomposition of foundry sand in a high-temperature environment.

The thermal decomposition kinetics parameters of foundry sand were obtained according to kinetics theory. The calculated thermal decomposition activation energy was higher in the air atmosphere than in the nitrogen atmosphere due to the presence of oxygen. To thoroughly test the fitting effects, we performed a single-factor analysis of variance on the source of error and found that the independent variable significantly influences the dependent variable.

Although this study achieved several significant results, to simplify the investigation, the binding materials used for the foundry sand only included furan resin. The thermal decomposition process of foundry sand may be different with different binding materials. Future work should focus on the influence of binding materials on the thermal decomposition process of foundry sand.

Data Availability

The thermal decomposition data supporting this paper have been uploaded as electronic supplementary materials.

Conflicts of Interest

The authors declare no conflicts of interest.

Authors' Contributions

Jinjia Zhang, Kaili Xu, and Qingwei Xu guided the writing process; Shoukun Chen, Jinjia Zhang, Kaili Xu, and Qingwei Xu conducted the experiments and data analysis; and Shoukun Chen wrote the paper. All the authors gave their final approval for publication.

Acknowledgments

This study was supported by the National Key Research and Development Program of China (no. 2018YFC0808406) and

the Fundamental Research Funds for the Central Universities (no. N180104018).

Supplementary Materials

The supplementary materials have been divided into four parts, and the corresponding concise descriptions of each supplementary material file are shown as follows. S1: thermal decomposition data of foundry sand at heating rate of 20°C/min in nitrogen. S2: thermal decomposition data of foundry sand at heating rate of 30°C/min in nitrogen. S3: thermal decomposition data of foundry sand at heating rate of 40°C/min in nitrogen. S4: thermal decomposition data of foundry sand at heating rate of 20°C/min in air. (*Supplementary Materials*)

References

- [1] J. Zhang, K. Xu, G. Reniers, and G. You, "Statistical analysis the characteristics of extraordinarily severe coal mine accidents (ESCMAs) in China from 1950 to 2018," *Process Safety and Environmental Protection*, vol. 133, pp. 332–340, 2020.
- [2] F. Yan and K. Xu, "A set pair analysis based layer of protection analysis and its application in quantitative risk assessment," *Journal of Loss Prevention in the Process Industries*, vol. 55, pp. 313–319, 2018.
- [3] J. Ge, K. Xu, X. Zheng, X. Yao, Q. Xu, and B. Zhang, "The main challenges of safety science," *Safety Science*, vol. 118, pp. 119–125, 2019.
- [4] Q. Xu, K. Xu, X. Yao, J. Zhang, and B. Wang, "Sand casting safety assessment for foundry enterprises: fault tree analysis, Heinrich accident triangle, HAZOP-LOPA, bow tie model," *Royal Society Open Science*, vol. 5, no. 10, p. 180915, 2018.
- [5] P. Zhao, Z.-l. Liu, G.-q. Wang, and P. Liu, "Casting process design and practice for coolant pump impeller in AP1000 nuclear power station," *China Foundry*, vol. 17, no. 2, pp. 173–177, 2020.
- [6] K. Hellström, V.-L. Diaconu, and A. Diószegi, "Density and thermal expansion coefficients of liquid and austenite phase in lamellar cast iron," *China Foundry*, vol. 17, no. 2, pp. 127–136, 2020.
- [7] S. A. Benromdhane, "Probabilistic risk-based pollution prevention model for a foundry: a case study of casting," *Environmental Science and Pollution Research*, vol. 25, no. 19, pp. 18332–18344, 2018.
- [8] M. Jozef, H. Emilia, L. Juraj, and B. Karol, "Environmental analysis of waste foundry sand via life cycle assessment," *Environmental Science and Pollution Research*, vol. 24, pp. 3153–3162, 2017.
- [9] Q. Xu and K. Xu, "Evaluation of ambient air quality based on synthetic cloud model," *Fresenius Environmental Bulletin*, vol. 27, pp. 141–146, 2018.
- [10] J. Li, K. Xu, B. Fan, and L. Geng, "Risk assessment of oxygen lance burning loss using bow-tie analysis based on fuzzy theory," *Mathematical Problems in Engineering*, vol. 2020, Article ID 7172184, 12 pages, 2020.
- [11] J. J. Mohammad, S. Fahimeh, A. Ebrahim, and Z. Farid, "Relationship between risk perception and occupational accidents: a study among foundry workers," *Journal of the Egyptian Public Health Association*, vol. 94, pp. 1–5, 2019.
- [12] L. Marmo, N. Piccinini, and L. Fiorentini, "Missing safety measures led to the jet fire and seven deaths at a steel plant in Turin. Dynamics and lessons learned," *Journal of Loss*

- Prevention in the Process Industries*, vol. 26, no. 1, pp. 215–224, 2013.
- [13] Q. Xu, K. Xu, L. Li, and X. Yao, “Optimization of sand casting performance parameters and missing data prediction,” *Royal Society Open Science*, vol. 6, no. 8, p. 181860, 2019.
- [14] S. Han, “Finite volume solution of two-step hyperbolic conduction in casting sand,” *International Journal of Heat and Mass Transfer*, vol. 93, pp. 1116–1123, 2016.
- [15] Q. Xu, K. Xu, L. Li, X. Xu, and X. Yao, “Energy release and countermeasures for sand casting explosion accidents,” *Human and Ecological Risk Assessment: An International Journal*, vol. 26, p. 1650327, 2019.
- [16] H. Dai, C. Zhang, Q. Zhao, and H. Zhu, “The study of titanium alloy precision casting turbine blades based on procast,” *IOP Conference Series: Materials Science and Engineering*, vol. 677, Article ID 022090, 2019.
- [17] S. Dubey and S. R. Swain, “Numerical investigation on solidification in casting using ProCAST,” *IOP Conference Series: Materials Science and Engineering*, vol. 561, Article ID 012049, 2019.
- [18] L. Zhang, W. Tan, and H. Hu, “Determination of the heat transfer coefficient at the metal-sand mold interface of lost foam casting process,” *Heat and Mass Transfer*, vol. 52, no. 6, pp. 1131–1138, 2015.
- [19] J. Wang, S.-y. Zhang, X. Guo et al., “Thermal behaviors and kinetics of pingshuo coal/biomass blends during copyrolysis and cocombustion,” *Energy & Fuels*, vol. 26, no. 12, pp. 7120–7126, 2012.
- [20] T. Fateh, T. Roguame, and F. Richard, “Multi-scale modeling of the thermal decomposition of fire retardant plywood,” *Fire Safety Journal*, vol. 64, pp. 36–47, 2014.
- [21] X. Yao, K. Xu, and Y. Liang, “Comparing the thermo-physical properties of rice husk and rice straw as feedstock for thermochemical conversion and characterization of their waste ashes from combustion,” *BioResource*, vol. 11, pp. 10579–10564, 2016.
- [22] F. Colangelo, G. De Luca, C. Ferone, and A. Mauro, “Experimental and numerical analysis of thermal and hygro-metric characteristics of building structures employing recycled plastic aggregates and geopolymer concrete,” *Energies*, vol. 6, no. 11, pp. 6077–6101, 2013.
- [23] M. Coronado, A. Andrés, and C. R. Cheeseman, “Acid gas emissions from structural clay products containing secondary resources: foundry sand dust and Waelz slag,” *Journal of Cleaner Production*, vol. 115, pp. 191–202, 2016.
- [24] I. N. Murthy and J. B. Rao, “Investigations on physical and chemical properties of high silica sand, Fe-Cr slag and blast furnace slag for foundry applications,” *Procedia Environmental Sciences*, vol. 35, pp. 583–596, 2016.
- [25] X. Yao, H. Zhou, K. Xu, Q. Xu, and L. Li, “Investigation on the fusion characterization and melting kinetics of ashes from co-firing of anthracite and pine sawdust,” *Renewable Energy*, vol. 145, pp. 835–846, 2020.
- [26] X. Yao, H. Zhou, K. Xu, S. Chen, J. Ge, and Q. Xu, “Systematic study on ash transformation behaviour and thermal kinetic characteristics during co-firing of biomass with high ratios of bituminous coal,” *Renewable Energy*, vol. 147, pp. 1453–1468, 2020.
- [27] Q. Xu, K. Xu, X. Yao, J. Li, and L. Li, “Thermal decomposition characteristics of foundry sand for cast iron in nitrogen atmosphere,” *Royal Society Open Science*, vol. 5, no. 12, p. 181091, 2018.
- [28] J. Ozoemenam, B. Akudinobi, V. Nnodu, and I. Obiadi, “Water quality assessment of shallow and deep boreholes in Ekpan community, Effurun, Delta State, Nigeria,” *Environmental Earth Sciences*, vol. 77, pp. 1–12, 2018.
- [29] M. Zhu, L. Liu, and Z. Wang, “Mesoporous silica via self-assembly of nano zinc amino-tris-(methylenephosphonate) exhibiting reduced fire hazards and improved impact toughness in epoxy resin,” *Journal of Hazardous Materials*, vol. 392, Article ID 122343, 2020.
- [30] Z. Huo, Q.-H. Wan, and L. Chen, “Energy-efficient and environment-friendly method to prepare monodispersed silica stationary phases for simultaneous separation of compound drugs,” *Journal of Chromatography A*, vol. 1618, Article ID 460866, 2020.
- [31] A. Mourhly, M. Kacimi, M. Halim, and S. Arsalane, “New low cost mesoporous silica (MSN) as a promising support of Ni-catalysts for high-hydrogen generation via dry reforming of methane (DRM),” *International Journal of Hydrogen Energy*, vol. 45, no. 20, pp. 11449–11459, 2020.
- [32] L. Xu, Y. Jiang, and L. Wang, “Thermal decomposition of rape straw: pyrolysis modeling and kinetic study via particle swarm optimization,” *Energy Conversion and Management*, vol. 146, pp. 124–133, 2017.
- [33] L. Mu, J. Chen, H. Yin, X. Song, A. Li, and X. Chi, “Pyrolysis behaviors and kinetics of refining and chemicals wastewater, lignite and their blends through TGA,” *Bioresour. Technology*, vol. 180, pp. 22–31, 2015.
- [34] X. Yao, K. Xu, and Y. Liang, “Assessing the effects of different process parameters on the pyrolysis behaviors and thermal dynamics of corncob fractions,” *Bioresour. Technology*, vol. 12, pp. 2748–2767, 2017.
- [35] H. C. Cheng, M. C. Chiu, C. M. Chiu, and C. Y. Yang, “Design and development of an automatic gas poisoning prevention and ventilation system,” *MATEC Web of Conferences*, vol. 185, Article ID 00010, 2018.
- [36] Y. Liu, X. Wang, X. Xu, W. Qin, and B. Sun, “Protective effects of carbon monoxide releasing molecule-2 on pancreatic function in septic mice,” *Molecular Medicine Reports*, vol. 19, p. 3449, 2019.
- [37] B. Samanta, T. Sengupta, and S. Pal, “Aluminum cluster for CO and O₂ adsorption,” *Journal of Molecular Modeling*, vol. 25, pp. 1–15, 2019.
- [38] H. M. Schipper, W. Song, A. Tavitian, and M. Cressatti, “The sinister face of heme oxygenase-1 in brain aging and disease,” *Progress in Neurobiology*, vol. 172, pp. 40–70, 2019.
- [39] S. H. Jang and H. G. Kwon, “Injury of ascending reticular activating system associated with delayed post-hypoxic leukoencephalopathy: a case report,” *BMC Neurology*, vol. 17, p. 139, 2017.
- [40] H. Zhang, H. Zhao, K. Zheng, X. Li, G. Liu, and Y. Wang, “Diminishing hazardous air pollutant emissions from pyrolysis of furan no-bake binders using methanesulfonic acid as the binder catalyst,” *Journal of Thermal Analysis and Calorimetry*, vol. 116, no. 1, pp. 373–381, 2014.
- [41] M. Holtzer, A. Kmita, S. Żymankowska-Kumon, A. Bobrowski, and R. Dańko, “Influence of the hardener on the emission of harmful substances from moulding sands with furan resin in the pyrolysis process,” *Archives of Foundry Engineering*, vol. 16, no. 1, pp. 107–111, 2016.
- [42] N. Guigo, A. Mija, R. Zavaglia, L. Vincent, and N. Sbirrazzuoli, “New insights on the thermal degradation pathways of neat poly (furfuryl alcohol) and poly (furfuryl alcohol)/SiO₂ hybrid materials,” *Polymer Degradation and Stability*, vol. 94, no. 6, pp. 908–913, 2009.
- [43] X. Yao, K. Xu, and Y. Liang, “Analytical pyrolysis study of peanut shells using TG-MS technique and characterization for

- the waste peanut shell ash,” *Journal of Residuals Science & Technology*, vol. 13, no. 4, pp. 295–305, 2016.
- [44] B. Tian, Y. Y. Qiao, Y. Y. Tian, and Q. Liu, “Investigation on the effect of particle size and heating rate on pyrolysis characteristics of a bituminous coal by TG-FTIR,” *Journal of Analytical and Applied Pyrolysis*, vol. 121, pp. 376–386, 2016.
- [45] Z. Diao, Y. Zhao, B. Chen, C. Duan, and S. Song, “ReaxFF reactive force field for molecular dynamics simulations of epoxy resin thermal decomposition with model compound,” *Journal of Analytical and Applied Pyrolysis*, vol. 104, pp. 618–624, 2013.
- [46] K. S. Chen and R. Z. Yeh, “Pyrolysis kinetics of epoxy resin in a nitrogen atmosphere,” *Journal of Hazardous Materials*, vol. 49, no. 2-3, pp. 105–113, 1996.
- [47] S. R. Chandrasekaran and P. K. Hopke, “Kinetics of switch grass pellet thermal decomposition under inert and oxidizing atmospheres,” *Bioresource Technology*, vol. 125, pp. 52–58, 2012.
- [48] C. Wu, J. You, and X. Wang, “Thermal decomposition mechanism and kinetics of gemcitabine,” *Journal of Analytical and Applied Pyrolysis*, vol. 130, pp. 118–126, 2018.
- [49] M. Yang, X. Chen, Y. Wang et al., “Comparative evaluation of thermal decomposition behavior and thermal stability of powdered ammonium nitrate under different atmosphere conditions,” *Journal of Hazardous Materials*, vol. 337, pp. 10–19, 2017.
- [50] W. Xie, S. Wen, J. Liu et al., “Comparative thermogravimetric analyses of co-combustion of textile dyeing sludge and sugarcane bagasse in carbon dioxide/oxygen and nitrogen/oxygen atmospheres: thermal conversion characteristics, kinetics, and thermodynamics,” *Bioresource Technology*, vol. 255, pp. 88–95, 2018.
- [51] J. Chen, C. Xie, J. Liu et al., “Co-combustion of sewage sludge and coffee grounds under increased O₂/CO₂ atmospheres: thermodynamic characteristics, kinetics and artificial neural network modeling,” *Bioresource Technology*, vol. 250, pp. 230–238, 2018.
- [52] L. Jiang, X. Yuan, H. Li et al., “Pyrolysis and combustion kinetics of sludge-camphor pellet thermal decomposition using thermogravimetric analysis,” *Energy Conversion and Management*, vol. 106, pp. 282–289, 2015.